Microscopic study of the production of neutron-rich isotopes near $N = 126$ in the multinucleon transfer reactions ^{78,82,86}Kr + ^{208}Pb

Yu-Hai Zhang [1,2] Jing-Jing Li,[3] Cheng Li,[4] Ming-Hao Zhang [1,2] Ying Zou [1,2] and Feng-Shou Zhang [1,2,5,*]

[1]*The Key Laboratory of Beam Technology of Ministry of Education, College of Nuclear Science and Technology,*
Beijing Normal University, Beijing 100875, China
[2]*Institute of Radiation Technology, Beijing Academy of Science and Technology, Beijing 100875, China*
[3]*College of Material Science and Technology, Nanjing University of Aeronautics and Astronautics, Nanjing 210016, China*
[4]*Department of Physics, Guangxi Normal University, Guilin 541004, China*
[5]*Center of Theoretical Nuclear Physics, National Laboratory of Heavy Ion Accelerator of Lanzhou, Lanzhou 730000, China*

The multinucleon transfer reactions ^{78,82,86}Kr + ^{208}Pb at near-barrier energy are investigated by the improved quantum molecular dynamics model with the subsequent decay model GEMINI. The isotopic distributions of the products in the ^{136}Xe + ^{208}Pb reaction at $E_{c.m.} = 450$ MeV are calculated and compared with the experimental data. The influence of isospin equilibration of the primary products in the ^{78,82,86}Kr + ^{208}Pb reactions are investigated. It suggests that the projectile ^{86}Kr is favorable to the yields of neutron-rich nuclei. The total kinetic energy mass distributions and the evolution of the neck in collisions of ^{86}Kr + ^{208}Pb at incident energies of $E_{lab} = 5.40$, 6.40, and 7.40 MeV/nucleon are calculated. By analyzing the incident energy effect on the mass distributions and isotopic distributions of products in the reaction of ^{86}Kr + ^{208}Pb, we find that 6.40 MeV/nucleon is more suitable for producing neutron-rich isotopes near $N = 126$.

I. INTRODUCTION

The investigation of unknown neutron-rich nuclei located near the neutron closed shell $N = 126$ has garnered considerable attention due to the desire to comprehend the astrophysical r-process path and the nuclear structure of extremely exotic nuclei [1]. The $N = 126$ shell closure is probably the last "waiting point" in the r-process and offers a nucleosynthesis mechanism for over half of the heavy nuclei present in the Universe [2,3]. The multinucleon transfer (MNT) reactions, which take place near the Coulomb barrier energy, have been suggested as a possible pathway to fill the "blank region" of the nuclide chart surrounding $N = 126$. For more comprehensive reviews, see Refs. [4–9].

Zagrebaev and Greiner firstly proposed that MNT reactions with ^{208}Pb target at near-barrier energies can produce the neutron-rich $N = 126$ nuclei based on multidimensional Langevin equations [10,11]. Subsequently, a large number of experiments using medium mass projectiles at energies near the Coulomb barriers were carried out to produce exotic nuclei near $N = 126$ [12–19]. For example, Comas *et al.* used a velocity filter SHIP for the separation of the heavy target-like transfer products in the ^{58,64}Ni + ^{207}Pb collisions at GSI [12,13]. Their experimental data revealed that most of the nuclei resulted from deep inelastic collisions with full dissipation of kinetic energy. In 2015, a major breakthrough in the production of new nuclides by the MNT process was achieved

when the reaction ^{48}Ca + ^{248}Cm was performed at GSI, leading to the discovery of five new neutron-deficient isotopes, including ^{216}U, ^{219}Np, ^{223}Am, ^{229}Am, and ^{233}Bk [14]. At the Grand Accelerateur National D'Ions Lourds (GANIL), the experimental results demonstrated that the production cross sections of nuclei along the $N = 126$ shell in the ^{136}Xe + ^{198}Pt reaction were significantly greater than those produced in projectile fragmentation [15]. Similarly, the MNT reaction ^{136}Xe + ^{208}Pb at $E_{c.m.} = 450$ MeV was carried out at Argonne National Laboratory (ANL), and it was discovered that the predicted yields of the neutron-rich $N = 126$ nuclei exceeded the measured values by 2 orders of magnitude for $\Delta Z = +4$ [16]. The mass distributions of the system ^{136}Xe + ^{208}Pb at laboratory energies near the Coulomb barrier were studied at JINR, and the time of flight(TOF)–TOF data were analyzed to reconstruct the mass-energy distribution of the primary fragments in the reaction of ^{136}Xe + ^{208}Pb [17,18]. Recently, a new isotope, ^{241}U, was synthesized and systematic atomic mass measurements of 19 neutron-rich Pa-Pu isotopes were carried out in MNT reactions of the ^{238}U + ^{198}Pt system at the KISS facility [19]. More experiments are planned to create heavy neutron-rich nuclei via MNT reactions at the Heavy Ion Research Facility in Lanzhou (HIRFL) and the High Intensity Heavy-Ion Accelerator Facility (HIAF) [20,21].

Numerous theoretical models have been proposed to describe MNT reactions near the Coulomb barrier. Semiclassical models, including the Grazing-F model [22], the Grazing model [23,24], multidimensional Langevin-type dynamical equations of motion [25–27], the complex WKB method

*Corresponding author: fszhang@bnu.edu.cn

[28–30], and the dinuclear system (DNS) model [31–50], are capable of predicting the production cross sections of unknown heavy and superheavy neutron-rich nuclei. The stochastic mean-field approach can also stimulate the multinucleon exchange in deep inelastic collisions [51–54]. The microscopic models [55,56], such as the time-dependent Hartree-Fock model and the improved quantum molecular dynamics (ImQMD) model, effectively elucidate the fusion [57–60] and transfer process mechanisms [61–70] and reasonably replicate the cross sections of the final products observed in experiments.

A deep understanding of the MNT mechanism and a reliable prediction of cross sections are helpful to choose optimal projectile-target combinations to produce new isotopes [9]. Several experiments have indicated that nuclides near $N = 126$ are more likely to be produced when neutron-rich nuclei are used as the projectile and the incident energy is close to the Coulomb barrier [11,25,71]. Hence, this work aims to investigate the nucleon transfer mechanisms, such as effects of isospin equilibration, energy dissipation, and the prediction of isotopic cross sections by employing the ImQMD model through ^{78,82,86}Kr + ^{208}Pb reactions at incident energies near 5–8 MeV/nucleon. The GEMINI model is used to treat the deexcitation process.

This paper is organized as follows. In Sec. II, we briefly introduce the ImQMD model. The results and discussion are presented in Sec. III. Finally, we summarize the main results in Sec. IV.

II. THE MODEL

The ImQMD model is an improved version of the quantum molecular dynamics (QMD) model [72,73]. To describe the fermionic nature of the N-body system and to improve the stability of an individual nucleus, the phase-space occupation constraint method is adopted [74]. The two-body collision correlations and the Pauli blocking checking are also included. Besides, the ImQMD model, based on the QMD model, not only updates the interaction potential but also introduces the initial wave-packet width dependent on the system size. Each nucleon is represented by a coherent state of a Gaussian wave pocket in the ImQMD model:

$$\phi_i(\mathbf{r}) = \frac{1}{(2\pi\sigma_r^2)^{3/4}} \exp\left[-\frac{(\mathbf{r} - \mathbf{r}_i)^2}{4\sigma_r^2} + \frac{i}{\hbar}\mathbf{r} \cdot \mathbf{p}_i\right], \quad (1)$$

where $\mathbf{r}_i$ and $\mathbf{p}_i$ are the centers of ith wave packet in the coordinate and momentum space, respectively. σ_r is the wave-packet width of a nucleon, which represents the spatial spread of the wave packet in coordinate space. The one-body phase-space distribution function is obtained by the Winger transform of the wave function. The propagation of nucleons

is governed by Hamiltonian equations of motion under the self-consistently generated mean field:

$$\dot{\mathbf{r}}_i = \frac{\partial H}{\partial \mathbf{p}_i}, \quad \dot{\mathbf{p}}_i = -\frac{\partial H}{\partial \mathbf{r}_i}. \quad (2)$$

The Hamiltonian H consists of the kinetic energy $T = \sum_i \frac{\mathbf{p}_i^2}{2m}$, the Coulomb interaction potential energy, and the nuclear interaction potential energy:

$$H = T + U_{\text{Coul}} + U_{\text{loc}}. \quad (3)$$

U_{Coul} is the Coulomb energy, which is expressed as

$$U_{\text{Coul}} = \frac{1}{2}\iint \rho_p(\mathbf{r})\frac{e^2}{|\mathbf{r} - \mathbf{r}'|}\rho_p(\mathbf{r}')d\mathbf{r}d\mathbf{r}'$$
$$- e^2\frac{3}{4}\left(\frac{3}{\pi}\right)^{1/3}\int \rho_p^{4/3}d\mathbf{r}. \quad (4)$$

Here, ρ_p is the density distribution of protons of the system. The nuclear interaction potential energy U_{loc} is obtained from the integration of the Skyrme energy density functional $U_{\text{loc}} = \int V_{\text{loc}}(\mathbf{r})d\mathbf{r}$ without the spin-orbit term, which reads

$$V_{\text{loc}} = \frac{\alpha}{2}\frac{\rho^2}{\rho_0} + \frac{\beta}{\gamma + 1}\frac{\rho^{\gamma+1}}{\rho_0^\gamma} + \frac{g_{\text{sur}}}{2\rho_0}(\nabla\rho)^2$$
$$+ \frac{C_s}{2\rho_0}[\rho^2 - \kappa_s(\nabla\rho)^2]\delta^2 + g_\tau\frac{\rho^{\eta+1}}{\rho_0^\eta}, \quad (5)$$

where $\rho = \rho_n + \rho_p$ is the nucleons density, and $\delta = (\rho_n - \rho_p)/(\rho_n + \rho_p)$ is the isospin asymmetry. The first three terms in the above expression are directly obtained from the Skyrme interaction. The fourth term denotes the symmetry potential energy including the bulk and surface symmetry potential energies. The last term is a small correction term.

In this work, we set the z axis as the beam direction and the x axis as the impact parameter direction. The initial distance of the center of mass between the projectile and the target is 30 fm. The wave-packet width is set as $\sigma_r = 1.2$ fm and the parameters named IQ2 (see Table I) are adopted in this work. The dynamic simulation is stopped at 1000 fm/c and 10 000 events for each impact parameter simulated. The range of impact parameters in the calculations is from 0 to b_{max} fm. $b_{\text{max}} = R_P + R_T$, where R_P and R_T denote the radii of the projectile and the target, respectively. In Fig. 1, we check the time evolution of binding energies for ^{78,82,86}Kr and ^{208}Pb calculated by the ImQMD model with the parameter set IQ2. One can see that their binding energies remain constant with a very small fluctuation and the bound nuclei evolve stably without spurious emission for a period of time of about 3000 fm/c, which is essential for applications to multinucleon transfer reactions.

TABLE I. Model parameters (IQ2) adopted in this work.

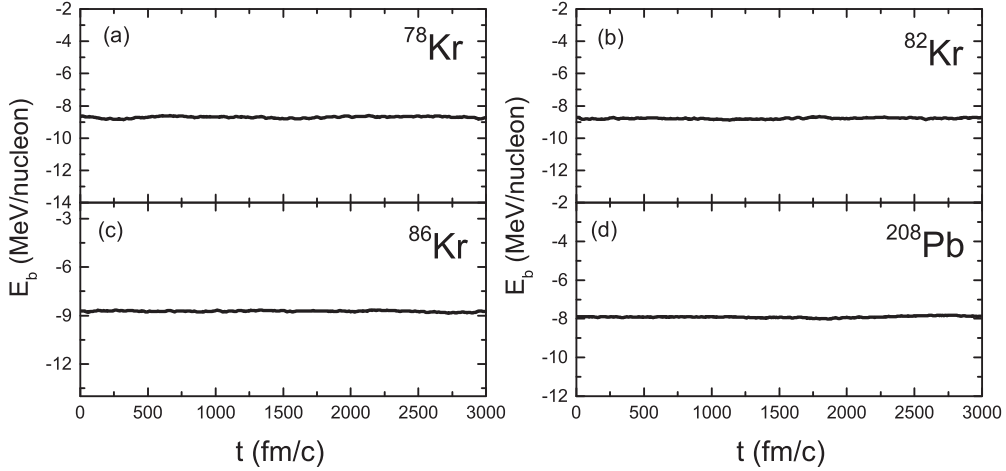| α (MeV)	β (MeV)	γ	g_{sur} (MeV fm^2)	g_τ (MeV)	η	C_S (MeV)	κ_s (fm^2)	ρ_0 (fm^{-3})
-356	303	7/6	7.0	12.5	2/3	32.0	0.08	0.165

FIG. 1. The time evolution of binding energies for ^{78,82,86}Kr and ^{208}Pb calculated by the ImQMD model with the parameter set IQ2.

Subsequently, the GEMINI code [75,76] is used to deal with the subsequent deexcitation process. The evaporation of the light particles is treated by Hauser-Feshbach theory and the level density in the GEMINI code is obtained by the Fermi gas expression [77]:

$$\rho(U, J) = (2J + 1)\left[\frac{\hbar^2}{2\mathcal{I}}\right]^{3/2}\frac{\sqrt{a}}{12}\frac{\exp(2\sqrt{aU})}{U^2}, \qquad (6)$$

where $\mathcal{I}$ is the moment-of-inertia of the residual nucleus or saddle-point configuration. The level density parameter was

taken as $a = A/8$ MeV^{-1} as usual, where A is the mass number of the excited nucleus.

Motivated by testing the reliability of using the combination of ImQMD with the GEMINI model, we present the production cross sections of nuclei with $Z = 78$–85 in the reaction ^{136}Xe $+ ^{208}$Pb at $E_{\text{c.m.}} = 450$ MeV in Fig. 2. The red solid circles represent the experimental data, which are obtained from Ref. [16]. In Fig. 2, it can be seen that the heights of peaks are consistent with experimental data for the combination of ImQMD with the GEMINI model. However, it overestimates the cross sections in the neutron-rich and
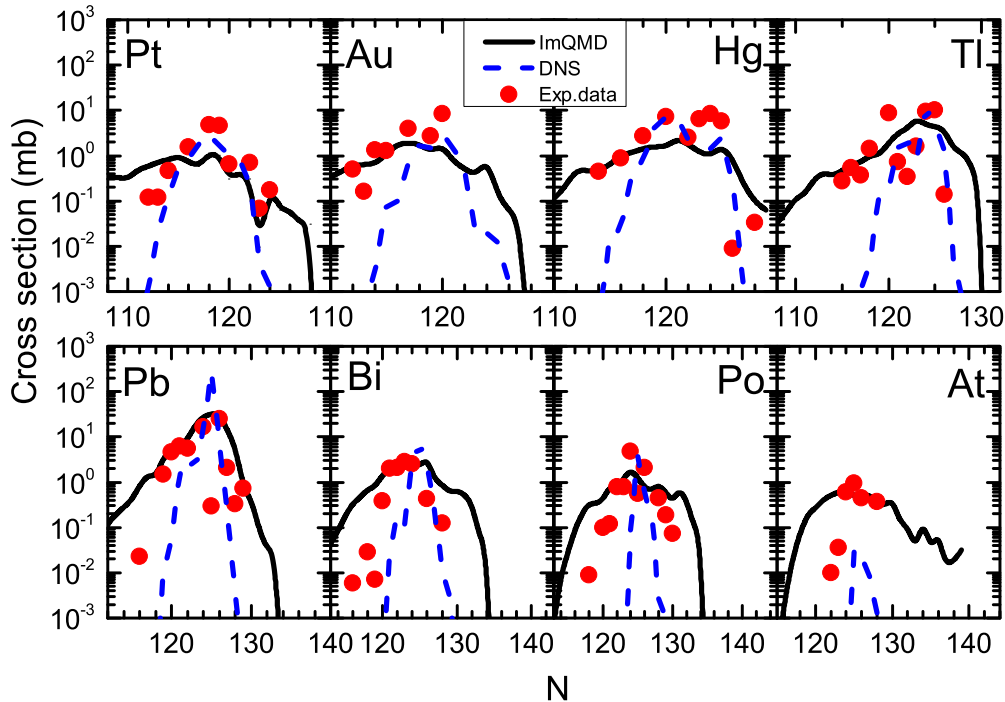

FIG. 2. The isotopic production cross sections from Pt to At in the reaction of ^{136}Xe $+ ^{208}$Pb at $E_{\text{c.m.}} = 450$ MeV. The black solid lines represent the calculations of the combination of ImQMD with the GEMINI model. The blue dashed lines denote the calculations of the combination of DNS with the GEMINI model. The red solid circles represent the experimental data, which are obtained from Ref. [16].
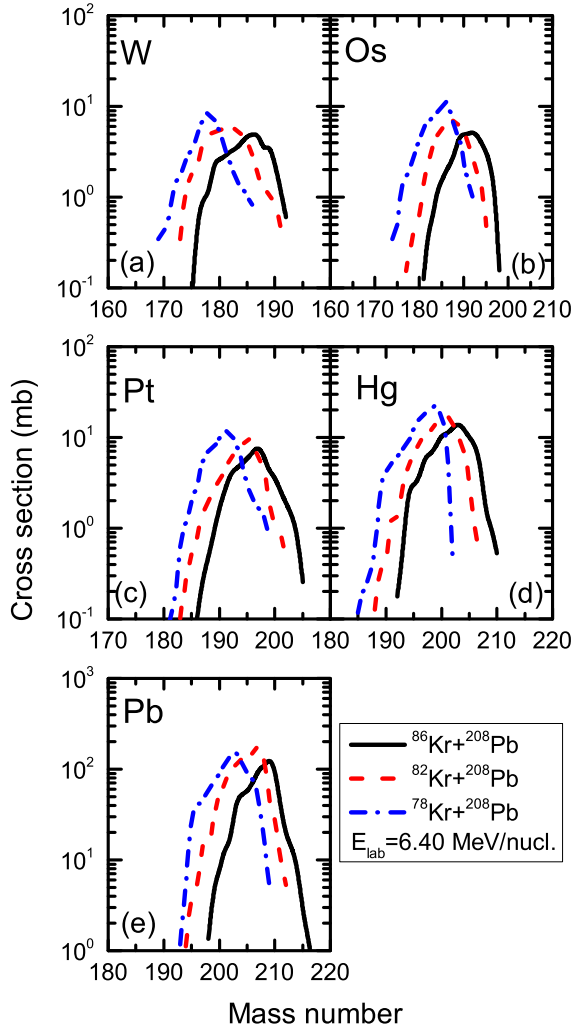
FIG. 3. The primary isotopic cross sections of (a) W, (b) Os, (c) Pt, (d) Hg, and (e) Pb in ^{78,82,86}Kr + ^{208}Pb three reactions at $E_{lab} = 6.40$ MeV/nucleon. The solid, dashed, and dash-dotted lines represent the results of ^{86}Kr + ^{208}Pb, ^{82}Kr + ^{208}Pb, and ^{78}Kr + ^{208}Pb, respectively.

neutron-deficient regions for the Bi, Po, and At cases. This is mainly because the experimental data in Ref. [16] are derived from intensities of a thick-target experiment not from direct particle identification. There are probably some differences between the two measurement methods for isotope production cross sections.

For the combination of DNS with the GEMINI model, the height of peaks is consistent with experimental data at least in an order of magnitude from Pt to Po. But in the case of describing larger proton transfer, such as At, the predictions by the DNS with the GEMINI model underestimate the experimental data at almost 2 orders of magnitude. Besides, the production cross sections decrease rapidly with increasing charge number in the vicinity of $Z > 82$. Moreover, it is lower than the experimental data in both the neutron-rich and the neutron-deficient regions. Overall, based on the above results, it is reasonable to apply the ImQMD with GEMINI method to describe the

isotopic distributions in the region near $N = 126$ via MNT reactions.

III. RESULTS AND DISCUSSION

A. Isospin equilibration

The isospin equilibration plays an important role between the projectile and the target during the collision, which is one of the most important mechanisms to produce neutron-rich nuclei [78]. Previous studies have shown that there is a transition from the isospin equilibrium at low energies to nonequilibration at high energies [79–81]. The primary isotopic cross sections of (a) W, (b) Os, (c) Pt, (d) Hg, and (e) Pb in the ^{78,82,86}Kr + ^{208}Pb three reactions at $E_{lab} = 6.40$ MeV/nucleon are shown in Fig. 3. The solid, dashed, and dash-dotted lines represent the results of ^{86}Kr + ^{208}Pb, ^{82}Kr + ^{208}Pb, and ^{78}Kr + ^{208}Pb, respectively. From Figs. 3(a)–3(e), one can see that the isotopic cross section becomes larger as the charge numbers of the fragments gradually approach the target. For instance, the peak of cross-section distribution of W is in the order of 10^0 to 10^1 mb [see Fig. 3(a)]. In contrast, for Pb, the peak of the isotopic cross-section distribution is reached in the range of 10^2 to 10^3 mb [see Fig. 3(e)]. This is mainly because the target nucleus ^{208}Pb has a relatively large N/Z ratio compared to the projectile, and nucleons transfer from the target to the projectile; thus the cross section of isotopes closer to the target is higher.

In Fig. 3, it is clear that the peaks for isotopic production cross sections decrease with increasing numbers of neutrons in the projectile for three reactions. The isotopic cross-section distributions of ^{86}Kr-induced reactions exhibit a shift towards the neutron-rich side when compared to the ^{78,82}Kr + ^{208}Pb reactions. This shift results in significant discrepancies in the cross section in the neutron-rich side. This is because the cross section in the neutron-rich side is very sensitive to the N/Z value of the projectile. The N/Z values for ^{78,82,86}Kr isotopes are 1.17, 1.28, and
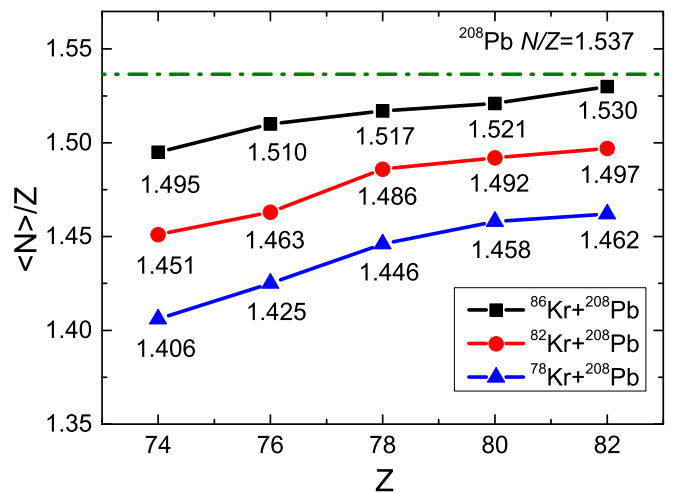

FIG. 4. The $\langle N \rangle /Z$ values for primary binary products of ^{78,82,86}Kr + ^{208}Pb at $E_{lab} = 6.40$ MeV/nucleon. The dashed line indicates the $\langle N \rangle /Z$ value of the target.
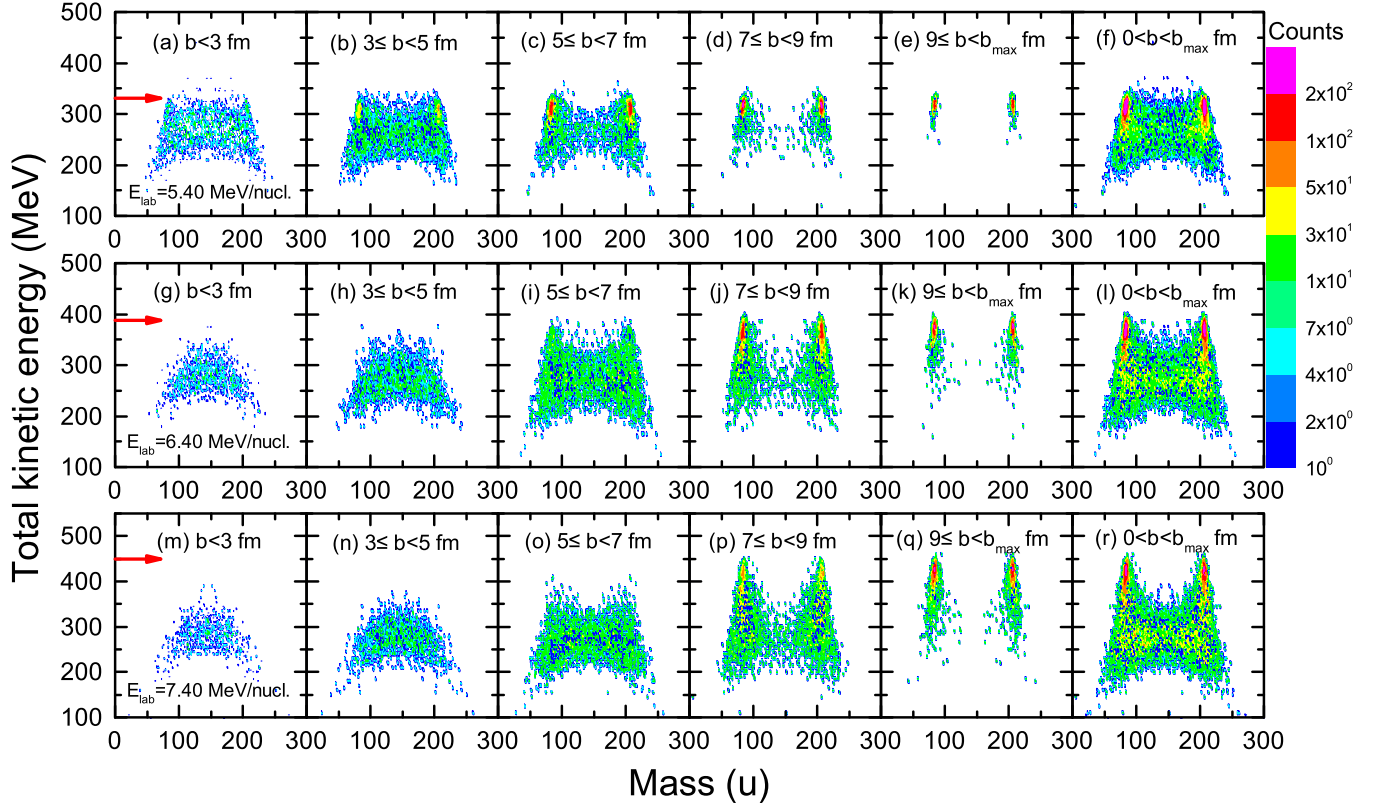
FIG. 5. TKE-mass distributions of primary fragments for the ^{86}Kr + ^{208}Pb reaction in different impact parameter regions at $E_{\text{lab}} =$ 5.40 MeV/nucleon (top panels), 6.40 MeV/nucleon (middle panels), and 7.40 MeV/nucleon (bottom panels), respectively. The red arrows denote the positions of different center-of-mass incident energies.

1.39, respectively. Therefore, the production cross section of neutron-rich isotopes in ^{86}Kr + ^{208}Pb are larger than those in the other two reactions. In comparison with ^{78,82}Kr + ^{208}Pb, the ^{86}Kr + ^{208}Pb system is more favorable to produce neutron-rich nuclei.

In heavy-ion collisions, there may be a significant disparity in the N/Z ratio between the target and the projectile. Typically, in collisions involving a heavy nucleus and a lighter partner, there is a tendency for the heavy nucleus to lose neutrons in order to achieve isospin equilibration [82]. The $\langle N \rangle/Z$ values for primary binary products of ^{78,82,86}Kr + ^{208}Pb at $E_{\text{lab}} = 6.40$ MeV/nucleon are shown in Fig. 4. The dashed line indicates the $\langle N \rangle/Z$ value of the target, and the mean neutron number for each Z can be obtained from $\langle N \rangle = \sum_i N_i \sigma_i / \sum_i \sigma_i$, where N_i and σ_i are the neutron number and the corresponding cross section, respectively [83].

From Fig. 4, one sees that the $\langle N \rangle/Z$ values of primary binary products increase rapidly with the increase of Z in the ^{78,82,86}Kr + ^{208}Pb reactions. Three-reaction systems are very close to the original target nuclei at $Z = 82$ with a N/Z ratio of 1.537. The discrepancy in $\langle N \rangle/Z$ is attributed to the difference N/Z of ^{78,82,86}Kr. This is mainly because there is a significant difference in the density distribution between neutrons and protons in the surface region of neutron-rich isotopes, and the isospin effect of the projectile is related to the density distribution of neutrons and protons. In Fig. 4, it also reveals that $\langle N \rangle/Z$ values of the fragment are higher with the increase of the neutron excess of the projectile. This suggests that more

neutron-rich nuclei can be produced in the MNT reaction for a given projectile with larger neutron excess, which is consistent with Refs. [84,85].

B. Energy dissipation

In MNT reactions, the collision mechanism of the reaction partners includes quasielastic, deep-inelastic, and quasifission reactions. Deep inelastic collisions between nuclei in contact lead to the profound reconstruction of the initial nuclei with incident energy dissipation. In the ImQMD frame, we distinguish the mechanism of the different collisions on the total kinetic energy (TKE) of primary fragments, which is express as

$$\text{TKE} = E_{\text{tot}} - \sum_k E_{\text{frag}}, \tag{7}$$

where $E_{\text{tot}} = E_{\text{c.m.}} + E_{\text{g.s.}}^{(1)} + E_{\text{g.s.}}^{(2)}$ denote the total energy of the reaction system at the initial time. $E_{\text{c.m.}}$ is the incident center-of-mass energy. $E_{\text{g.s.}}^{(1)}$ and $E_{\text{g.s.}}^{(2)}$ are the ground-state energies of the projectile and the target nucleus, respectively. E_{frag} denotes the energy of an outgoing fragment in its center-of-mass frame, which is expressed as£º

$$E_{\text{frag}} = \sum_i \frac{(\mathbf{p}_i - \mathbf{p}_c)^2}{2m} + U, \tag{8}$$

where $\mathbf{p}_i$ and $\mathbf{p}_c$ denote the momentum of each nucleon in the fragment and the collective momentum of a fragment,
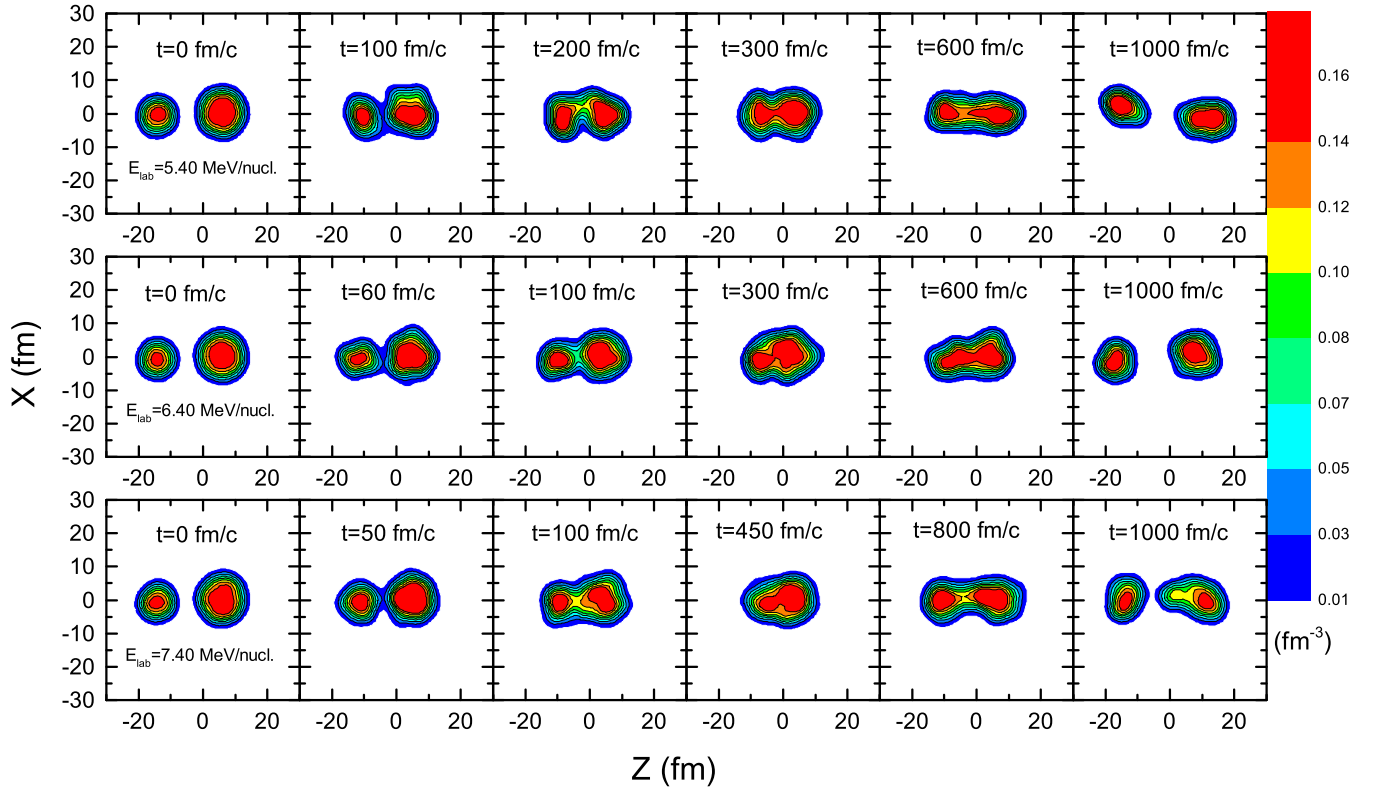
FIG. 6. Time evolution of density distribution of the projectilelike and targetlike fragments in the MNT reaction ^{86}Kr $+$ ^{208}Pb with the impact parameter $b = 1$ fm at three incident energies: $E_{lab} = 5.40$ MeV/nucleon (top panels), $E_{lab} = 6.40$ MeV/nucleon (middle panels), and $E_{lab} = 7.40$ MeV/nucleon (bottom panels).

respectively. U denoted the interaction potential energy of a fragment, which can be calculated from $U = U_{Coul} + U_{loc}$ [see Eqs. (4) and (5)].

The TKE-mass distributions of primary binary fragments for the ^{86}Kr $+$ ^{208}Pb reaction at three incident energies are shown in Fig. 5. In the ImQMD model, the evolution of the system is carried out in the overall center-of-mass reference frame. The red arrows denote the positions of different center-of-mass incident energies.

From Fig. 5, one can see three behaviors.

(i) TKE-mass distribution in central collisions is quite different from those in peripheral collisions. In central collisions [Figs. 5(a), 5(g), and 5(m)], the TKE has a decreasing trend with the increasing incident energy. While the TKE-mass distribution is less sensitive to incident energy in peripheral collisions [Figs. 5(e), 5(k), and 5(q)].

(ii) The TKE increases with increasing impact parameters for a particular incident energy. Taking the TKE-mass distribution at $E_{lab} = 6.40$ MeV/nucleon as an example, it can be seen that the TKE is located in the region of 200–340 MeV for $b < 3$ fm [Fig. 5(g)]. The corresponding energy dissipation is about 190–50 MeV, which indicates that most deep-inelastic events take place in central collisions. For $3 \leqslant b < 5$ fm [Fig. 5(h)] and $5 \leqslant b < 7$ fm [Fig. 5(i)], the TKE is distributed over a wide range from 200–350 MeV.

This demonstrates deep inelastic and quasielastic collision events occur simultaneously in semicentral and semiperipheral collisions. For $b \geqslant 7$ fm [Figs. 5(j) and 5(k)], the TKE is gradually close to 390 MeV. This means the probability of binary quasielastic events increases, which results in small energy dissipation.

(iii) The masses of fragments are distributed in a rather broad range for $0 < b < 7$ fm. This is because the neck of the dinuclear system can be well formed and quickly broadened and many nucleons are transferred between the projectile and the target in central to semiperipheral collisions. However, the region of TKE-mass distribution for $7 \leqslant b < b_{max}$ fm is narrow due to the decrease of nucleon transfer in the peripheral collision.

As mentioned above in Fig. 5, the incident energy effect is very sensitive to central collisions. To further understand the influence of nucleon transfer on the TKE of fragments, we investigate the time evolution of density distribution for the collisions of the ^{86}Kr $+$ ^{208}Pb reaction with the impact parameter $b = 1$ fm at three incident energies in Fig. 6. Because the deformation effects of reaction partners are not considered self-consistently in ImQMD simulations, the sampled initial nuclei are spherical in shape. One can see that the contact time between the projectile and the target decrease with increasing of incident energies. The projectile-target contact time can
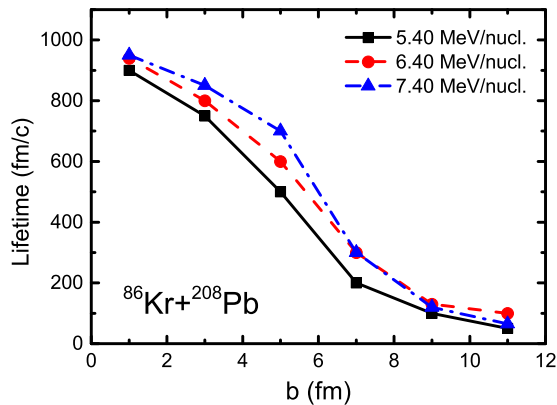
FIG. 7. Lifetime of the neck calculated by the ImQMD model as a function of impact parameters. The solid, dashed, and dash-dotted lines represent the results of $E_{lab} = 5.40$, 6.40, and 7.40 MeV/nucleon, respectively.

be estimated as 100, 60, and 50 fm/c at $E_{lab} = 5.40$, 6.40, and 7.40 MeV/nucleon, respectively. Nevertheless, the projectilelike and targetlike fragments' separation time is about 1000 fm/c at all three energies.

From Fig. 6, the lifetime of the neck should be defined as from the projectile and target contacting time to the separation time. Therefore, the lifetime of the neck is determined to be about 900, 940, and 950 fm/c at $E_{lab} = 5.40$, 6.40, and 7.40 MeV/nucleon, respectively. As the incident energies rise, the extent of nucleon exchange between the projectile and the target is also extended, leading to an increased lifetime of the neck.

By studying the nucleon exchange, we extracted the lifetime of the neck at three different energies with impact parameters of $b = 1, 3, 5, 7, 9,$ and 11 in Fig. 7. The solid, dashed, and dash-dotted lines represent the results of $E_{lab} = 5.40$, 6.40, and 7.40 MeV/nucleon, respectively. One can see that neck lifetimes decrease with increasing impact parameters due to the contribution of the angular momentum of system. The slope in the region of $b < 7$ fm is larger than that in the region of $b \geqslant 7$ fm. This indicates that the nucleon transfer mostly occurs in the central collision region as well as in the semiperipheral collision region, which is also consistent with Fig. 5.

From Fig. 7, it also can be seen that in the region of $b < 7$ fm, the lifetime of the neck at $E_{lab} = 7.40$ MeV/nucleon is the longest compared to the other two energies. While in the region of $b \geqslant 7$ fm, the lifetime of the neck is not sensitive to the incident energy. This is because a large number of elastic and inelastic scattering events are produced in the region of $b \geqslant 7$ fm, which makes it hard for the system to form the neck.

C. Production cross sections of neutron-rich isotopes near $N = 126$

To study the effect of dynamic fluctuation on the transfer mass distribution, the mass distributions of primary binary fragments in the MNT reaction of $^{86}Kr + ^{208}Pb$ are shown in Fig. 8. Figure 8(a) displays the cross sections with all impact parameters at three incident energies, it is obvious

that more nucleons are transferred with increasing incident energy. However, the mass distributions of primary binary fragments at three incident energies are very close at the double-peak positions. Besides, it is also noticed that the cross-section distributions exhibit a wide range of 170 mass units. This suggests that a large number of nucleon transfer between the projectile and the target at the incident energy near the Coulomb barrier.

The mass distributions of primary fragments at different impact parameters b are calculated to clarify the origin of the fragments with different mass regions. Figures 8(b)–8(f) show the results of the $^{86}Kr + ^{208}Pb$ reaction at $E_{lab} = 6.40$ MeV/nucleon for the impact parameters of $0 < b < 3$, $3 \leqslant b < 5$, $5 \leqslant b < 7$, $7 \leqslant b < 9$, and $9 \leqslant b < b_{max}$ fm, respectively. In Fig. 8(b), it is evident that the primary cross sections are generally low for the region of $0 < b < 3$ fm, probably in the order of 10^0–10^1 mb. This is because the excitation energy of this system is higher at small collision parameters, and there are many sequential fission events occurring. Compared to Fig. 8(b), the mass distribution in Fig. 8(c) exhibits a broader range. The mass distribution displays two distinct peaks, attributed to Kr and Pb, with values ranging from 10^1–10^2 mb.

From Figs. 8(d) and 8(e), it is obvious that the fragments near the projectile and the target are mainly the products of the semiperipheral and peripheral collisions. The middle region of the two curves is located at about $A = 140$, and the middle value of the semiperipheral collision is about 10^0 mb, while the middle values of the peripheral collisions are between 10^0 and 10^1 mb. This is because the incident energy is slightly higher than the Coulomb barrier, and the quasielastic scattering makes an important contribution in this region.

In Figs. 8(d)–8(f), it is clear that the cross sections of the mass of the entrance channel decrease gradually with increasing impact parameters. In Fig. 8(f), one can see that there are two peaks at $A = 86$ and $A = 208$, with cross section values of 10.222 and 6.239 mb, respectively.

To obtain the optimal incident energy for producing the neutron-rich heavy nuclei, Fig. 9 shows the distributions of secondary isotopic fragments for (a) Pt, (b) Hg, (c) Pb, and (d) Po in the reaction of $^{86}Kr + ^{208}Pb$ at three different incident energies. The red dashed lines, black solid lines, and blue dash-dotted lines denote the calculated results for $E_{lab} = 5.40$ MeV/nucleon, $E_{lab} = 6.40$ MeV/nucleon, and $E_{lab} = 7.40$ MeV/nucleon, respectively. The solid circles represent the $N \geqslant 126$ neutron-rich isotopes produced at $E_{lab} = 6.40$ MeV/nucleon. From Fig. 9, one can see that the isotopic production cross sections become higher with increasing incident energies in the neutron-deficient side, because the larger incident energy improves the transfer probability of nucleons, which leads to a larger production cross section for the primary neutron-deficient nuclei.

In Fig. 9, it is obvious that the optimal incident energy for producing the neutron-rich nuclei near $N = 126$ is 6.40 MeV/nucleon. The production cross sections of the neutron-rich nuclei increase firstly and then decrease with the increasing incident energy. For the case of $E_{lab} = 5.40$ MeV/nucleon, the production cross sections of the primary neutron-rich nuclei are lower. For the case of
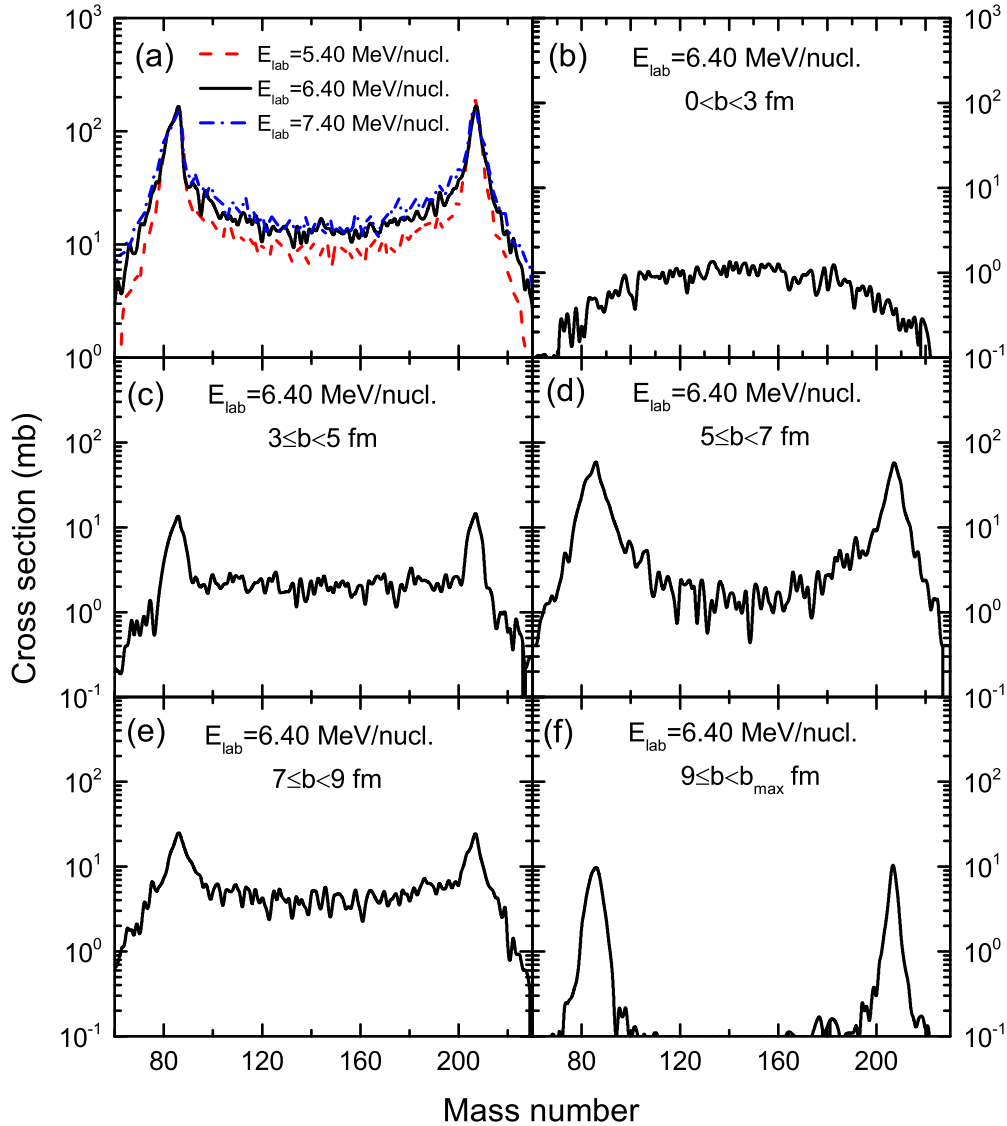
FIG. 8. (a) Mass distributions of primary binary fragments in the reaction of ^{86}Kr $+$ ^{208}Pb at three incident energies. The dashed, solid, and dash-dotted lines denote the calculated values of $E_{lab} = 5.40$, 6.40, and 7.40 MeV/nucleon, respectively. The mass distributions of primary binary fragments in the reaction of ^{86}Kr $+$ ^{208}Pb at $E_{lab} = 6.40$ MeV/nucleon for impact parameters (b) $0 < b < 3$ fm, (c) $3 \leqslant b < 5$ fm, (d) $5 \leqslant b < 7$ fm, (e) $7 \leqslant b < 9$ fm, and (f) $9 \leqslant b < b_{max}$ fm, respectively.

$E_{lab} = 7.40$ MeV/nucleon, the primary products are highly excited, leading to a lower survival probability for the neutron-rich nuclei. Besides, there is a bell-shaped distribution of Pb ($Z = 82$) in Fig. 9(c). The peak of the isotopic production cross section is located at $N = 126$. This is because the fragments located at $N = 126$ mainly came from the contribution of quasielastic collisions where the primary products have low excitation energies. As mentioned above, the incident energy of 6.40 MeV/nucleon in the ^{86}Kr $+$ ^{208}Pb reaction is favorable for the production of neutron-rich isotopes.

Table II shows the production cross sections of predicted known isotopes with $N \geqslant 126$. The measured experimental cross sections are obtained in the reaction of ^{58}Ni $+$ ^{208}Pb [78]. From Table II, it is obvious that the yields become lower with more neutrons transferred at the same incident energy.

Compared with the experimental data of the ^{58}Ni $+$ ^{208}Pb reaction system at $E_{lab} = 345$ MeV, it is evident that both the theoretical and experimental cross sections are in the order of 10^2 mb for the production of ^{208}Pb. For the production of ^{210}Po and ^{212}Po, these results are in the order of 10^1 mb for the former isotope and 10^{-1}–10^0 mb for the latter.

In Table II, it is also clear that the predicted isotopes with higher neutron excess are ^{204}Pt, ^{210}Hg, ^{216}Pb, and ^{218}Po, and the corresponding cross sections are 6.57, 3.65, 67.56, and 0.942 μb, respectively.

IV. CONCLUSIONS

The multinucleon transfer mechanisms for the reactions ^{78,82,86}Kr $+$ ^{208}Pb at near-barrier energies were studied by using the ImQMD model with the GEMINI code. This model
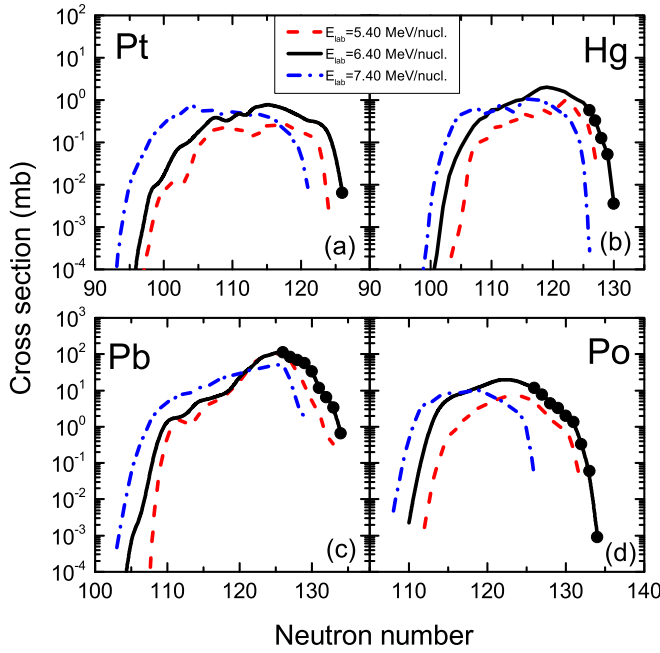
FIG. 9. The distributions of secondary isotopic fragments for (a) Pt, (b) Hg, (c) Pb, and (d) Po in the reaction of ^{86}Kr + ^{208}Pb at three different incident energies. The red dashed lines, black solid lines, and blue dash-dotted lines denote the calculated results for $E_{lab} = 5.40$ MeV/nucleon, $E_{lab} = 6.40$ MeV/nucleon, and $E_{lab} = 7.40$ MeV/nucleon, respectively. The solid circles represent the $N \geqslant 126$ neutron-rich isotopes produced at $E_{lab} = 6.40$ MeV/nucleon.

TABLE II. The production cross sections of predicted known isotopes with $N \geqslant 126$ in the ^{86}Kr + ^{208}Pb transfer reaction at $E_{lab} = 6.40$ MeV/nucleon. The measured experimental cross sections are obtained in the reaction of 345-MeV ^{58}Ni + ^{208}Pb [78].

Isotope	N	$\sigma_{cal.}^{^{86}Kr+^{208}Pb}$/mb	$\sigma_{exp.}^{^{58}Ni+^{208}Pb}$/mb
^{204}Pt	126	6.570×10^{-3}	
^{206}Hg	126	5.697×10^{-1}	
^{207}Hg	127	3.266×10^{-1}	
^{208}Hg	128	1.262×10^{-1}	
^{209}Hg	129	5.293×10^{-2}	
^{210}Hg	130	3.650×10^{-3}	
^{208}Pb	**126**	**115.402**	**120 [78]**
^{209}Pb	127	86.025	
^{210}Pb	128	70.333	
^{211}Pb	129	58.109	
^{212}Pb	130	33.701	
^{213}Pb	131	12.098	
^{214}Pb	132	6.719	
^{215}Pb	133	3.436	
^{216}Pb	134	6.756×10^{-2}	
^{210}Po	**126**	**12.128**	**14.4 [78]**
^{211}Po	127	7.915	
^{212}Po	**128**	**4.501**	**0.3 [78]**
^{213}Po	129	3.372	
^{214}Po	130	2.033	
^{215}Po	131	1.372	
^{216}Po	132	3.327×10^{-1}	
^{217}Po	133	6.136×10^{-2}	
^{218}Po	134	9.425×10^{-4}	

can well reproduce the transfer reaction cross sections of nuclei near $N = 126$ in the ^{136}Xe + ^{208}Pb reaction. In comparison with ^{78,82}Kr + ^{208}Pb reactions, the larger production cross sections of neutron-rich isotopes can be obtained by the ^{86}Kr-induced reaction due to the large neutron excess in the projectile.

The TKE-mass distributions of primary binary fragments in different impact parameter regions and different incident energies are given, and the results show that the deep inelastic events occur in the central collision region, and quasielastic scattering occurs mainly in the peripheral collision region. The TKE-mass distribution has a decreasing trend with the increasing incident energy in the central collisions, but it is less sensitive to the incident energy in peripheral collisions. The lifetime of the neck plays an important role in the nucleon exchange and energy dissipation between the projectile and the target during the collisions. The lifetime of the neck decreases with increasing impact parameters and increases with increasing incident energy. The fragments near the projectile

and the target are mainly the products of the semiperipheral and peripheral collisions.

The influence of the incident energy on the yield of targetlike fragments in the ^{86}Kr + ^{208}Pb reaction is also studied. To produce neutron-rich isotopes near the $N = 126$ region, the optimal incident energy is $E_{lab} = 6.40$ MeV/nucleon in the ^{86}Kr + ^{208}Pb reaction. The predicted cross sections for isotopes with higher neutron excess, ^{204}Pt, ^{210}Hg, ^{216}Pb, and ^{218}Po, are 6.57, 3.65, 67.56, and 0.942 μb, respectively.

[1] S. Heinz and H. M. Devaraja, Eur. Phys. J. A **58**, 114 (2022).

[2] J. J. Cowan, F. K. Thielemann, and J. W. Truran, Phys. Rep. **208**, 267 (1991).

[3] K. Langanke and M. Wiescher, Rep. Prog. Phys. **64**, 1657 (2001).

[4] W. D. Loveland, Front. Phys. **7**, 23 (2019).

[5] L. Corradi, G. Pollarolo, and S. Szilner, J. Phys. G: Nucl. Part. Phys. **36**, 113101 (2009).

[6] F. S. Zhang, C. Li, L. Zhu, and P. W. Wen, Front. Phys. **13**, 1 (2018).

[7] F. S. Zhang, Y. H. Zhang, M. H. Zhang, N. Tang, S. H. Cheng, J. J. Li, and W. Cheng, J. Beijing Normal Univ. (Nat. Sci.) **58**, 392 (2022).

[8] Y. H. Zhang, G. Zhang, J. J. Li, W. Cheng, and F. S. Zhang, J. Isot. **35**, 104 (2022).

[9] J. J. Li, N. Tang, Y. H. Zhang, M. H. Zhang, C. Wang, X. R. Zhang, L. Zhu, and F. S. Zhang, Int. J. Mod. Phys. E **32**, 2330002 (2023).

[10] V. Zagrebaev and W. Greiner, J. Phys. G: Nucl. Part. Phys. **34**, 1 (2007).

[11] V. Zagrebaev and W. Greiner, Phys. Rev. Lett. **101**, 122701 (2008).

[12] V. F. Comas, S. Heinz, S. Hofmann, D. Ackermann, J. A. Heredia, F. P. Heßberger, J. Khuyagbaatar, B. Kindler, B. Lommel, and R. Mann, Eur. Phys. J. A **49**, 112 (2013).

[13] O. Beliuskina, S. Heinz, V. Zagrebaev, V. Comas, C. Heinz, S. Hofmann, R. Knöbel, M. Stahl, D. Ackermann, F. P. Heßberger, B. Kindler, B. Lommel, J. Maurer, and R. Mann, Eur. Phys. J. A **50**, 161 (2014).

[14] H. Devaraja, S. Heinz, O. Beliuskina, V. Comas, S. Hofmann, C. Hornung, G. Münzenberg, K. Nishio, D. Ackermann, Y. Gambhir, M. Gupta, R. Henderson, F. Heßberger, J. Khuyagbaatar, B. Kindler, B. Lommel, K. Moody, J. Maurer, R. Mann, A. Popeko *et al.*, Phys. Lett. B **748**, 199 (2015).

[15] Y. X. Watanabe, Y. H. Kim, S. C. Jeong, Y. Hirayama, N. Imai, H. Ishiyama, H. S. Jung, H. Miyatake, S. Choi, J. S. Song, E. Clement, G. de France, A. Navin, M. Rejmund, C. Schmitt, G. Pollarolo, L. Corradi, E. Fioretto, D. Montanari, M. Niikura *et al.*, Phys. Rev. Lett. **115**, 172503 (2015).

[16] J. S. Barrett, W. Loveland, R. Yanez, S. Zhu, A. D. Ayangeakaa, M. P. Carpenter, J. P. Greene, R. V. F. Janssens, T. Lauritsen, E. A. McCutchan, A. A. Sonzogni, C. J. Chiara, J. L. Harker, and W. B. Walters, Phys. Rev. C **91**, 064615 (2015).

[17] E. M. Kozulin, E. Vardaci, G. N. Knyazheva, A. A. Bogachev, S. N. Dmitriev, I. M. Itkis, M. G. Itkis, A. G. Knyazev, T. A. Loktev, K. V. Novikov, E. A. Razinkov, O. V. Rudakov, S. V. Smirnov, W. Trzaska, and V. I. Zagrebaev, Phys. Rev. C **86**, 044611 (2012).

[18] D. Quero, E. Vardaci, E. M. Kozulin, V. A. Zagrebaev, L. Corradi, A. Pulcini, G. L. Rana, I. M. Itkis, G. N. Knyazheva, K. Novikov, I. Harca, E. Fioretto, A. M. Stefanini, D. Montanari, G. Montagnoli, F. Scarlassara, S. Szilner, T. Mijatovic, and W. H. Trzaska, J. Phys.: Conf. Ser. **1014**, 012015 (2018).

[19] T. Niwase, Y. X. Watanabe, Y. Hirayama, M. Mukai, P. Schury, A. N. Andreyev, T. Hashimoto, S. Iimura, H. Ishiyama, Y. Ito, S. C. Jeong, D. Kaji, S. Kimura, H. Miyatake, K. Morimoto, J. Y. Moon, M. Oyaizu, M. Rosenbusch, A. Taniguchi, and M. Wada, Phys. Rev. Lett. **130**, 132502 (2023).

[20] L. J. Mao, J. C. Yang, J. W. Xia, X. D. Yang, Y. J. Yuan, J. Li, X. M. Ma, T. Yan, D. Y. Yin, W. P. Chai, L. N. Sheng, G. D. Shen, H. Zhao, and M. T. Tang, Nucl. Instrum. Methods Phys. Res., Sect. A **786**, 91 (2015).

[21] L. N. Sheng, X. H. Zhang, J. Q. Zhang, J. C. Yang, Z. Y. Sun, L. J. Mao, W. Wu, D. Y. Yin, S. Ruan, G. D. Shen, W. P. Chai, M. Wang, X. W. Ma, X. H. Zhou, J. W. Xia, H. W. Zhao, and G. Q. Xiao, Nucl. Instrum. Methods Phys. Res., Sect. B **469**, 1 (2020).

[22] R. Yanez and W. Loveland, Phys. Rev. C **91**, 044608 (2015).

[23] A. Winther, Nucl. Phys. A **572**, 191 (1994).

[24] A. Winther, Nucl. Phys. A **594**, 203 (1995).

[25] V. I. Zagrebaev and W. Greiner, Phys. Rev. C **83**, 044618 (2011).

[26] V. I. Zagrebaev and W. Greiner, Phys. Rev. C **87**, 034608 (2013).

[27] V. V. Saiko and A. V. Karpov, Phys. Rev. C **99**, 014613 (2019).

[28] E. Vigezzi and A. Winther, Ann. Phys. **192**, 432 (1989).

[29] L. Corradi, J. H. He, D. Ackermann, A. M. Stefanini, A. Pisent, S. Beghini, G. Montagnoli, F. Scarlassara, G. F. Segato, G. Pollarolo, C. H. Dasso, and A. Winther, Phys. Rev. C **54**, 201 (1996).

[30] L. Corradi, A. M. Stefanini, D. Ackermann, S. Beghini, G. Montagnoli, C. Petrache, F. Scarlassara, C. H. Dasso, G. Pollarolo, and A. Winther, Phys. Rev. C **49**, R2875 (1994).

[31] V. V. Volkov, Phys. Rep. **44**, 93 (1978).

[32] G. G. Adamian, N. V. Antonenko, R. V. Jolos, and W. Scheid, Nucl. Phys. A **619**, 241 (1997).

[33] G. G. Adamian, N. V. Antonenko, S. M. Lukyanov, and Y. E. Penionzhkevich, Phys. Rev. C **78**, 024613 (2008).

[34] G. G. Adamian, N. V. Antonenko, and D. Lacroix, Phys. Rev. C **82**, 064611 (2010).

[35] M. H. Mun, G. G. Adamian, N. V. Antonenko, Y. Oh, and Y. Kim, Phys. Rev. C **89**, 034622 (2014).

[36] M. H. Mun, K. Kwak, G. G. Adamian, and N. V. Antonenko, Phys. Rev. C **99**, 054627 (2019).

[37] M. H. Mun, K. Kwak, G. G. Adamian, and N. V. Antonenko, Phys. Rev. C **101**, 044602 (2020).

[38] Z. Q. Feng, Phys. Rev. C **95**, 024615 (2017).

[39] X. J. Bao, S. Q. Guo, and P. H. Chen, Phys. Rev. C **105**, 024610 (2022).

[40] J. J. Li, G. Zhang, X. R. Zhang, Y. H. Zhang, Z. Liu, and F. S. Zhang, J. Phys. G: Nucl. Part. Phys. **49**, 025106 (2022).

[41] J. J. Li, N. Tang, Y. H. Zhang, X. R. Zhang, G. Zhang, and F. S. Zhang, Phys. Rev. C **106**, 014606 (2022).

[42] G. Zhang, C. Li, P. W. Wen, J. J. Li, X. X. Xu, B. Li, Z. Liu, and F. S. Zhang, Phys. Rev. C **98**, 014613 (2018).

[43] G. Zhang, C. A. T. Sokhna, Z. Liu, and F. S. Zhang, Phys. Rev. C **100**, 024613 (2019).

[44] G. Zhang, J. J. Li, X. R. Zhang, B. Li, C. A. T. Sokhna, C. Wang, Z. Liu, and F. S. Zhang, Phys. Rev. C **102**, 024617 (2020).

[45] X. R. Zhang, G. Zhang, J. J. Li, S. H. Cheng, Z. Liu, and F. S. Zhang, Phys. Rev. C **103**, 024608 (2021).

[46] L. Zhu, J. Su, C. Li, and F. S. Zhang, Phys. Lett. B **829**, 137113 (2022).

[47] L. Zhu and J. Su, Phys. Rev. C **104**, 044606 (2021).

[48] N. Tang, X. R. Zhang, J. J. Li, P. W. Wen, and F. S. Zhang, Phys. Rev. C **106**, 034601 (2022).

[49] Z. H. Liao, L. Zhu, J. Su, and C. Li, Phys. Rev. C **107**, 014614 (2023).

[50] Y. H. Zhang, J. J. Li, N. Tang, X. R. Zhang, Z. Liu, and F. S. Zhang, Phys. Rev. C **107**, 024604 (2023).

[51] S. Ayik, O. Yilmaz, B. Yilmaz, and A. S. Umar, Phys. Rev. C **100**, 044614 (2019).

[52] S. Ayik, B. Yilmaz, O. Yilmaz, and A. S. Umar, Phys. Rev. C **102**, 024619 (2020).

[53] S. Ayik, M. Arik, E. C. Karanfil, O. Yilmaz, B. Yilmaz, and A. S. Umar, Phys. Rev. C **104**, 054614 (2021).

[54] S. Ayik, M. Arik, O. Yilmaz, B. Yilmaz, and A. S. Umar, Phys. Rev. C **107**, 014609 (2023).

[55] H. Wolter, M. Colonna, D. Cozma, P. Danielewicz, C. M. Ko, R. Kumar, A. Ono, M. B. Tsang, J. Xu, Y. X. Zhang, E. Bratkovskaya, Z. Q. Feng, T. Gaitanos, A. Le Fèvre, N. Ikeno,

Y. Kim, S. Mallik, P. Napolitani, D. Oliinychenko, T. Ogawa *et al.*, Prog. Part. Nucl. Phys. **125**, 103962 (2022).

[56] M. Colonna, Y. X. Zhang, Y. J. Wang, D. Cozma, P. Danielewicz, C. M. Ko, A. Ono, M. B. Tsang, R. Wang, H. Wolter, J. Xu, Z. Zhang, L. W. Chen, H. G. Cheng, H. Elfner, Z. Q. Feng, M. Kim, Y. Kim, S. Jeon, C. H. Lee *et al.*, Phys. Rev. C **104**, 024603 (2021).

[57] X. X. Sun and L. Guo, Phys. Rev. C **107**, 064609 (2023).

[58] N. Wang, Z. X. Li, and X. Z. Wu, Phys. Rev. C **65**, 064608 (2002).

[59] N. Wang, L. Ou, Y. X. Zhang, and Z. X. Li, Phys. Rev. C **89**, 064601 (2014).

[60] Y. H. Zhang, G. Zhang, J. J. Li, Z. Liu, A. V. Yeremin, and F. S. Zhang, Phys. Rev. C **106**, 014625 (2022).

[61] K. Sekizawa, Front. Phys. **7**, 20 (2019).

[62] Z. J. Wu, L. Guo, Z. Liu, and G. X. Peng, Phys. Lett. B **825**, 136886 (2022).

[63] B. J. Roy, S. Santra, A. Pal, H. Kumawat, S. K. Pandit, V. V. Parkar, K. Ramachandran, K. Mahata, and K. Sekizawa, Phys. Rev. C **105**, 044611 (2022).

[64] J. L. Tian, X. Z. Wu, K. Zhao, Y. X. Zhang, and Z. X. Li, Phys. Rev. C **77**, 064603 (2008).

[65] K. Zhao, Z. Liu, F. S. Zhang, and N. Wang, Phys. Lett. B **815**, 136101 (2021).

[66] K. Zhao, Z. X. Li, X. Z. Wu, and Y. X. Zhang, Phys. Rev. C **88**, 044605 (2013).

[67] C. Li, P. W. Wen, J. J. Li, G. Zhang, B. Li, X. X. Xu, Z. Liu, S. F. Zhu, and F. S. Zhang, Phys. Lett. B **776**, 278 (2018).

[68] C. Li, J. L. Tian, and F. S. Zhang, Phys. Lett. B **809**, 135697 (2020).

[69] X. Jiang and N. Wang, Phys. Rev. C **101**, 014604 (2020).

[70] C. Li, F. Zhang, J. J. Li, L. Zhu, J. L. Tian, N. Wang, and F. S. Zhang, Phys. Rev. C **93**, 014618 (2016).

[71] A. V. Karpov and V. V. Saiko, Phys. Rev. C **96**, 024618 (2017).

[72] J. Aichelin, Phys. Rep. **202**, 233 (1991).

[73] N. Wang, Z. X. Li, X. Z. Wu, J. L. Tian, Y. X. Zhang, and M. Liu, Phys. Rev. C **69**, 034608 (2004).

[74] M. Papa, T. Maruyama, and A. Bonasera, Phys. Rev. C **64**, 024612 (2001).

[75] R. J. Charity, M. A. McMahan, G. J. Wozniak, R. J. McDonald, L. G. Moretto, D. G. Sarantites, L. G. Sobotka, G. Guarino, A. Pantaleo, L. Fiore, A. Gobbi, and K. D. Hildenbrand, Nucl. Phys. A **483**, 371 (1988).

[76] R. J. Charity, Phys. Rev. C **82**, 014610 (2010).

[77] W. Hauser and H. Feshbach, Phys. Rev. **87**, 366 (1952).

[78] W. Królas, R. Broda, B. Fornal, T. Pawłat, J. Wrzesiński, D. Bazzacco, G. de Angelis, S. Lunardi, R. Menegazzo, D. Napoli, and C. R. Alvarez, Nucl. Phys. A **832**, 170 (2010).

[79] B. A. Li and S. J. Yennello, Phys. Rev. C **52**, R1746 (1995).

[80] L. W. Chen, F. S. Zhang, G.-M. Jin, and Z.-Y. Zhu, Phys. Lett. B **459**, 21 (1999).

[81] L. W. Chen, F. S. Zhang, and G. M. Jin, Phys. Rev. C **58**, 2283 (1998).

[82] L. Zhu, C. Li, C. C. Guo, J. Su, P. W. Wen, G. Zhang, and F. S. Zhang, Int. J. Mod. Phys. E **29**, 2030004 (2020).

[83] X. H. Zhang, Z. Y. Sun, R. F. Chen, Z. Q. Chen, Z. Y. Guo, J. L. Han, Z. G. Hu, T. H. Huang, R. S. Mao, Z. G. Xu, M. Wang, J. S. Wang, Y. Wang, G. Q. Xiao, H. S. Xu, X. H. Yuan, H. B. Zhang, X. Y. Zhang, and T. C. Zhao, Phys. Rev. C **85**, 024621 (2012).

[84] Z. Cheng and X. J. Bao, Phys. Rev. C **103**, 064613 (2021).

[85] C. Li, C. A. T. Sokhna, X. Xu, J. J. Li, G. Zhang, B. Li, Z. S. Ge, and F. S. Zhang, Phys. Rev. C **99**, 034619 (2019).